Boosting MPD Thruster Propulsion Efficiency through Optimization

IEPC-2009-229

Masao Nagao[*]
Nihon University, Funabashi, Chiba, 274-8501, Japan

Kenichi Kubota[†]
Japan Aerospace Exploration Agency, Sagamihara, Kanagawa, 229-8510, Japan

Masakatsu Nakane[‡] and Yoshio Ishikawa[§]
Nihon University, Funabashi, Chiba, 274-8501, Japan

and

Ikkoh Funaki[¶]
Japan Aerospace Exploration Agency, Sagamihara, Kanagawa, 229-8510, Japan

Abstract: Many researchers look to magnetoplasmadynamic (MPD) thrusters to power future manned space missions. This class of thrusters has a low thrust efficiency, therefore, which has hindered its practical realization. One of the strategies for improving performance is to refine the shape of its discharge chamber. The authors propose a method for optimizing the shape of the discharge chamber of a self-field MPD thruster, using a 2-dimensional axially symmetric model of plasma flow. This method was used to optimize the chamber, in which the anode was limited to flared shapes, and was shown to be valid.

Nomenclature

z	=	axial coordinate
r	=	radial coordinate
ρ	=	mass density
$\mathbf{u}$	=	velocity
p	=	pressure
$\overline{\overline{\tau}}$	=	viscous stress tensor
$\mathbf{j}$	=	current density
$\mathbf{B}$	=	magnetic flux density
ε	=	energy density
$\mathbf{E}$	=	electric field
λ	=	thermal conductivity
T	=	temperature

[*] Graduate Student, Department of Aerospace Engineering, nagao@stone.aero.cst.nihon-u.ac.jp
[†] Researcher, Institute of Space and Astronautical Science, Kubota@gd.isas.jaxa.jp
[‡] Assistant, Department of Aerospace Engineering, m_nak@stone.aero.cst.nihon-u.ac.jp
[§] Professor, Department of Aerospace Engineering, yishi@stone.aero.cst.nihon-u.ac.jp
[¶] Associate Professor, Institute of Space and Astronautical Science, funaki@isas.jaxa.jp

I	=	unit tensor
μ_0	=	magnetic permeability
σ	=	electrical conductivity
γ	=	specific heat ratio
α	=	ionization degree
$\dot{m}$	=	mass flow rate
J	=	discharge current
V	=	discharge voltage
η	=	thrust efficiency
F	=	thrust
S	=	area element vector
l	=	line element vector
L_a	=	overall length of discharge chamber
L_{st}	=	anode straight section length
L_c	=	cathode length
r_{in}	=	inlet anode radius
r_{out}	=	outlet anode radius
r_c	=	cathode radius
L_t	=	cathode tip cone length
θ	=	diverging angle
P	=	design variable vector

I. Introduction

THE MPD thruster features one of the highest thrust densities of all electric thrusters and will be easy to scale up in size and power output. Many look to the MPD thruster to serve as the main engine for future missions to Mars. One of the issues in realizing such engines, however, is the low thrust efficiency of this thruster. One approach to improving efficiency is to vary the cross sectional shape of the discharge chamber. Researchers in institutes all over the world have experimented with a wide variety of shapes, but have yet to identify clear-cut principles for designing the discharge chamber. On the other hand, Toki[1] showed in numerical simulations using mathematical programming that a converging-diverging chamber reaches a high thrust efficiency for a quasi-1-dimensional flow field and a constant input power.

We are studying the optimization of the discharge chamber cross-sectional shape in a self-field MPD thruster, using a 2-dimensional axially symmetric plasma model. Our goal is to identify clear design guidelines. Such optimization has not been feasible in the past, due to the high calculation cost involved in computational fluid dynamics (CFD). However, in this paper we propose a unique approach to optimization, combining with the response surface method with a Kriging model[2] to reduce the calculation load with a differential evolution algorithm to carry out the optimization efficiently.

A condensed version of Kubota's analytical code[3] was used to solve example problems involving a flared nozzle, which is commonly used in experiments on discharge chamber shapes. This optimization method was shown to be effective when carried out under the assumptions given below.

II. Modeling

A. Assumptions of Flowfield

The following assumptions were made in this CFD analysis of 2-dimensional axially symmetric plasma flow in the MPD thruster.

· The flow field is a single fluid model in 2-dimensional axially symmetric.
· The propellant was assumed as a fully ionized plasma of Ar^+.
· Thermal conductance and fluid viscosity were accounted for.
· Sheath hall voltage was a constant 20 V.
· Multi-step ionization and the Hall effect were neglected.
· The nozzle walls were perfect insulators.
· Heat equilibrium was preserved locally.

2

· Single temperature model was assumed.

B. Governing Equations
The followings are the governing equations defining the flow inside the MPD thruster, if all of the above assumptions hold true.

Mass conservation law

$$\frac{\partial \rho}{\partial t} + \nabla \cdot (\rho \mathbf{u}) = 0 \tag{1}$$

Momentum equation

$$\frac{\partial \rho \mathbf{u}}{\partial t} + \nabla \cdot (\rho \mathbf{u}\mathbf{u} + p\mathbf{I}) = \mathbf{j} \times \mathbf{B} + \nabla \cdot \overline{\tau} \tag{2}$$

Energy conservation law

$$\frac{\partial \varepsilon}{\partial t} + \nabla \cdot \left[(\varepsilon + p)\mathbf{u} \right] = \mathbf{j} \cdot \mathbf{E} + \nabla \cdot (\overline{\tau}\mathbf{u}) + \nabla \cdot (\lambda \nabla T) \tag{3}$$

Equation of state

$$p = (1 + \alpha)\rho RT \tag{4}$$

Ohm's law

$$\mathbf{j} = \sigma (\mathbf{E} + \mathbf{u} \times \mathbf{B}) \tag{5}$$

Maxwell's equation

$$\nabla \times \mathbf{B} = \mu_0 \mathbf{j} \tag{6}$$

Induction equation of magnetic field

$$\frac{\partial \mathbf{B}}{\partial t} = \nabla \times (\mathbf{u} \times \mathbf{B}) - \nabla \times \left(\frac{1}{\sigma \mu_0} \nabla \times \mathbf{B} \right) \tag{7}$$

Here, the internal energy ε and viscosity tensor $\overline{\tau}$ are obtained as follows:

$$\varepsilon = \frac{1}{2}\rho \mathbf{u} + \frac{p}{\gamma - 1} \tag{8}$$

$$\overline{\tau}_{ij} = \mu \left[\left(\frac{\partial u_i}{\partial x_j} - \frac{\partial u_j}{\partial x_i} \right) - \frac{2}{3}\delta_{ij}\frac{\partial u_k}{\partial x_k} \right] \tag{9}$$

The values for the thermal conductivity coefficient λ, electrical conductivity σ and viscosity coefficient μ were found in the Reference[3]. The degree of ionization was constant at $\alpha = 1$ due to the assumption of a fully ionized plasma.

C. Numerical Method
The TVD Lax-Friedrich scheme was employed to solve governing equations (1)-(3). The characteristic magnetic field diffusion time was far shorter than the time needed for changes in the flow, so magnetic field diffusion was considered steady. The Induction equation of magnetic field (7) was solved at each time step using successive over-relaxation (SOR).

D. Calculation Conditions
The calculation conditions were set as follows taking into consideration the actual operating conditions:

Table 1. Calculation Conditions

Propellant	Argon
Mass flow rate $\dot{m}$ [g/s]	0.8
Discharge current J [kA]	8.0
Inlet temperature T_{in} [K]	10000
Sheath hall voltage [V]	20
Mesh size	120 x 40

Thus, in this study, the key operating parameter of MPD thruster performance assessment was set as $J^2/\dot{m} = 8.0 \times 10^{10} A^2 s/kg$. The settings of the boundary condition etc. other than Table 1 refer to Reference[3].

3

III.   Formulation of Optimization Problem

E. Evaluated Value

The purpose of this study was to improve thrust efficiency, so the evaluated value to be assessed and maximized was defined as follows:

$$\eta = \frac{F^2}{2\dot{m}P} = \frac{F^2}{2\dot{m}JV} \tag{10}$$

The thrust F was calculated by integrating the momentum flux across the outlet:

$$F = \int_{\text{outlet}} \left(\rho \mathbf{u}\mathbf{u} + p\mathbf{I} \right) \cdot d\mathbf{S} \tag{11}$$

The discharge voltage V was calculated by line-integrating the electric field for the voltage drop between the anode and the cathode. This was added to the constant sheath hall voltage of 20 V to find the final value.

$$V = \int_{\text{anode}}^{\text{cathode}} \mathbf{E} \cdot d\mathbf{l} + 20 = \int_{\text{anode}}^{\text{cathode}} \left(\frac{\mathbf{j}}{\sigma} - \mathbf{u} \times \mathbf{B} \right) \cdot d\mathbf{l} + 20 \tag{12}$$

This analysis did not account for the Hall effect or other phenomena, so it underestimates the true discharge voltage and overestimates the true thrust efficiency.

F. Design Variables

The design variables are the shape parameters of the discharge chamber, which, in this optimization process, were limited to flared shapes. The followings describe the acceptable ranges for each shape parameter.

Table 2. Discharge chamber shape parameters

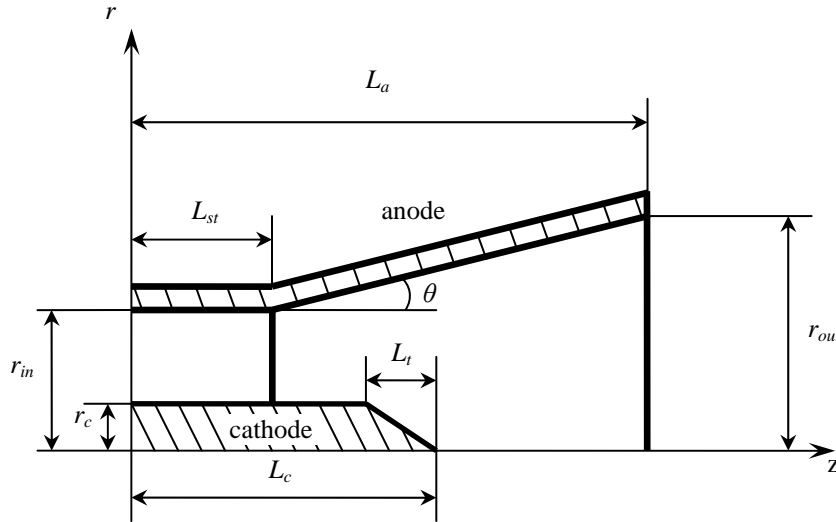|	
Chamber overall length L_a [cm]	$2.0 \le L_a \le 6.0$
Length of straight section L_{st} [cm]	$0.4 \le L_{st} \le 4.0$
Cathode length L_c [cm]	$1.0 \le L_c \le 4.8$
Inlet anode radius r_{in} [cm]	$0.7 \le r_{in} \le 2.0$
Outlet anode radius r_{out} [cm]	$1.0 \le r_{out} \le 3.5$

Figure 1. Discharge chamber shape

The cathode radius r_c was set at 0.4 cm and the length of the conical section at the tip of the cathode was set at L_t = 0.7 cm. Thus, there were 5 design variables in this study: L_a, L_{st}, L_c, r_{in} and r_{out}.

G. Constraints for Design Variables

The following constraints were applied to the design variables.

Table 3. Constraints

Cathode length/Discharge chamber overall length	$L_c/L_a \leq 4/5$
Straight section length/Discharge chamber overall length	$L_{st}/L_a \leq 2/3$
Diverging angle θ [deg]	$5 \leq \theta \leq 30$

where the diverging angle is defined by

$$\theta = \tan^{-1}\left(\frac{L_a - L_{st}}{r_{out} - r_{in}}\right) \tag{13}$$

IV. Kriging Model

We used the response surface method with the Kriging model to optimize the chamber shape. The response surface method expresses the relation between a design variable and a calculated evaluated value in an approximation equation, using some selected sampled points. Specifically, we employed an approximation equation to express the relation between discharge chamber shape and thrust efficiency. This approach allowed us to reduce the number of CFD calculations, greatly reducing the time needed to achieve the optimization.

The Kriging model was originally developed as a procedure for geostatistics to describe and predict the spatial distribution of mineral resources. In recent years, this was applied as the model of the approximation equation in the response surface method[4,5,6]. One characteristic of the Kriging model is that it interpolates the sample points mutually and makes the approximation equation, using a concept of the indeterminacy. In other words, it is well suited for use in computer experiments, where measurement errors do not occur.

In the Kriging model, the evaluated values $y(\mathbf{P})$ of the design variables $\mathbf{P} = [L_a \ L_{st} \ L_c \ r_{in} \ r_{out}]^T$ are taken as the actual values of the stochastic variables from the stochastic field. They are defined as follows[6]:

$$y(\mathbf{P}) = f(\mathbf{P}) + Z(\mathbf{P}) \tag{14}$$

where $f(\mathbf{P})$ is the global model and $Z(\mathbf{P})$ is a stochastic process expressing the error with respect to $f(\mathbf{P})$, which has a mean value of zero but has a non-zero covariance:

$$COV\left[Z(\mathbf{P}_i), Z(\mathbf{P}_j)\right] = k^2 \mathbf{R} \tag{15}$$

It is assumed that this stochastic process is generally stationary.

$\mathbf{R}$ in Eq. (15) is an n x n correlation matrix and is found with the following expression; n is the number of sample points.

$$R_{ij} = R(\mathbf{P}_i, \mathbf{P}_j) = \exp\left[-\sum_{h=1}^{m} \beta_h \left(\mathbf{P}_i - \mathbf{P}_j\right)_h^2\right] \tag{16}$$

Here, m is the number of design variables and β_h are parameters with values that are more than zero.

$f(\mathbf{P})$ in Eq. (14) is generally handled as a constant; if so, the best unbiased estimator for $y(\mathbf{P})$ of the design variables $\mathbf{P}$ is

$$\hat{y}(\mathbf{P}) = \hat{f} + \mathbf{r}^T \mathbf{R}^{-1}\left(\mathbf{y} - \mathbf{1}\hat{f}\right) \tag{17}$$

where

$$\mathbf{y} = \left[y(\mathbf{P}_1) \quad y(\mathbf{P}_2) \quad \cdots \quad y(\mathbf{P}_n)\right]^T \tag{18}$$

$$\hat{f} = \frac{\mathbf{1}^T \mathbf{R}^{-1} \mathbf{y}}{\mathbf{1}^T \mathbf{R}^{-1} \mathbf{1}} \tag{19}$$

$$\mathbf{r} = \left[R(\mathbf{P}, \mathbf{P}_1) \quad R(\mathbf{P}, \mathbf{P}_2) \cdots \quad R(\mathbf{P}, \mathbf{P}_n)\right]^T \tag{20}$$

In the above, $\mathbf{1}$ represents an n-dimensional vector whose components are all equal to unity.

Also, the value for β_h in Eq. (16) is defined as that which maximizes the following likelihood function L:

$$L = -\frac{n}{2}\log\hat{\kappa}^2 - \frac{1}{2}\log(det\mathbf{R}) \tag{21}$$

where

$$\hat{\kappa}^2 = \frac{\left(\mathbf{y} - \mathbf{1}\hat{f}\right)^T \mathbf{R}^{-1}\left(\mathbf{y} - \mathbf{1}\hat{f}\right)}{n} \tag{22}$$

In the Kriging model, the mean squared error of the predicted value $\hat{y}(\mathbf{P})$ can be predicted[2]:

$$s^2 = \hat{\kappa}^2 \left[1 - \mathbf{r}^T \mathbf{R}^{-1} \mathbf{r} + \frac{\left(1 - \mathbf{1}^T \mathbf{R}^{-1} \mathbf{r}\right)^2}{\mathbf{1}^T \mathbf{R}^{-1} \mathbf{1}} \right] \tag{23}$$

the minimum value of this is zero, when $\mathbf{P}$ matches exactly with the sample points. The further $\mathbf{P}$ is from the sample points, the greater the value of s^2.

V.   Optimization Process

H. Flow Chart
Figure 2 depicts the flow chart of the optimization process in the response surface method. This section explains the details of the flow.
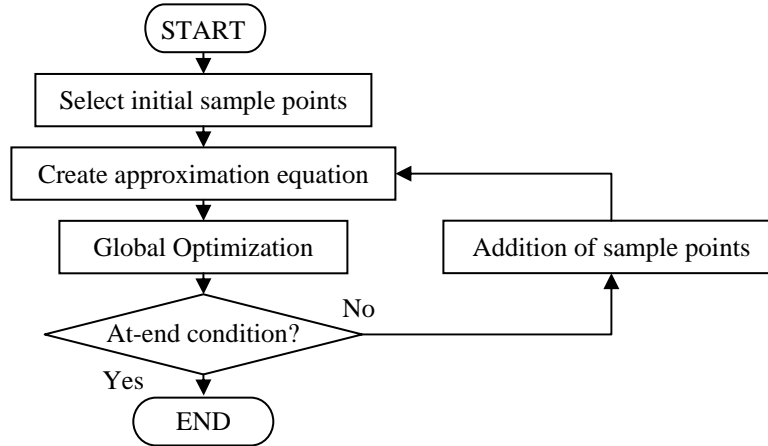
Figure 2. Flow chart of optimization process

I.   Selection of Initial Sampling Points
The basic purpose of the Kriging model is for interpolating between sample points to obtain a predicted value for any arbitrary point $\mathbf{P}$. In order to establish the response surface, therefore, it is vital to place sample points in the solution space so as to gain as much information about the solution space as possible. An experimental design was used to satisfy that requirement. Experimental design was originally developed for making efficient examinations of the extent of influence of factors and their interactions; under the response surface method, they can be applied to find out appropriate arrangement of the samples.
In this study, Latin Hypercube Sampling[7], one of the experimental designs, was employed to identify sample points on 88 discharge chamber shapes.

J. Global Optimization
It has been stated above that the Kriging model provides an approximation equation for interpolating between sample points; in other words, this suggests that the possibility that the solution space obtained using this equation becomes multimodal. Therefore, global optimization of the approximation equation obtained is necessary, and the optimization procedure taken in this study employed a Differential Evolution (DE)[8]:
The DE was solved as follows:
[1] N design variables were generated at random and evaluated.
[2] Target design variable $\mathbf{P}_t$ was selected at random.
[3] Design variables $\mathbf{P}_a$, $\mathbf{P}_b$ and $\mathbf{P}_c$ were selected at random. All of $\mathbf{P}_t$, $\mathbf{P}_a$, $\mathbf{P}_b$ and $\mathbf{P}_c$ were design variables.
[4] Design variables $\mathbf{P}_a$, $\mathbf{P}_b$ and $\mathbf{P}_c$ were mutated at the mutation ratio G (0.0 < G < 2.0) to create the vector $\mathbf{V}$.

$$\mathbf{V} = \mathbf{P}_a + \mathrm{G}\left(\mathbf{P}_b - \mathbf{P}_c\right) \tag{24}$$

[5] The new design variable $\mathbf{P}_{new}$ was created using $\mathbf{P}_t$ and $\mathbf{V}$ according to the crossover ratio CR ($0.0 < \mathrm{CR} < 1.0$).

[6] Either $\mathbf{P}_t$ or $\mathbf{P}_{new}$ was left to the next generation by comparing their adaptability.

[7] Steps [1] - [6] were repeated until the at-end condition was reached.

This procedure was used in the present study to find the β_h parameter of the Kriging model.

K. Addition of Sample points

Generally, it is difficult to develop an accurate approximation equation with only initial sample points. Therefore, in this study, the new optimal values selected with the DE created from the approximation equation were added as new sample points. The approximation equation was then revised and the DE was used to search for new optimal values in a repeat of the previous step, providing steady improvements in accuracy of the approximation equation. Thus, this was a process of sequential approximate optimization.

This study also employed the Expected Improvement (EI) function. The value provided by the approximation equation for the thrust efficiency under design variable vector $\mathbf{P}$ was represented by $\hat{y}$, the maximum value satisfying the constraints within the number of sample points was η_{max}, and the error in predictions that could be provided by Eq. (23) was represented by s. These were used to define the EI function:

$$\mathrm{EI} = \left(\hat{y} - \eta_{max}\right)\Phi\left[\frac{\hat{y} - \eta_{max}}{s}\right] + s\phi\left[\frac{\hat{y} - \eta_{max}}{s}\right] \tag{25}$$

where $\Phi[\cdot]$ was the cumulative density distribution of the normal distribution and $\phi[\cdot]$ was the probability density function of the normal distribution.

This EI is an index that expresses the potential for the thrust efficiency to be improved beyond the sample points obtained. EI is used as the evaluated value and can enable both efficient improvement of the approximation equation and global searches for optimum solution[2].

Ninety shapes were added as additional samples in this study.

L. Estimation of Discharge Voltage

It has been experimentally shown that the greater the input power provided to the MPD thruster, the better its thrust efficiency[9]. Thus, in order to observe the influence of the effectiveness of discharge chambers alone, it is preferable to conduct the optimization under the condition of constant input power. Constant current sources, which allow the current to be specified, have been used in experiments with MPD thrusters. Still, it is not possible to know the discharge voltage until the thruster has begun to fire. This is also true in CFD simulations, which only show the voltage after the calculations have converged.

Therefore, besides thrust efficiency, this study employed the Kriging model to observe the discharge voltage. An approximation equation was developed to calculate this value $\hat{v}$, and this enabled us to conduct optimization while making rough estimates of the voltage. We were able to make approximate guesses of the voltage without carrying out CFD calculations, so avoiding unnecessary CFD simulations with chamber shapes that would not satisfy the necessary voltage conditions. The approximation equation for $\hat{v}$ was also employed to develop constraints that contributed to optimizing the chamber shape for constant input power. The discharge voltage was set to v^*, we defined the constraints $\hat{v} \le v^*$ and $\hat{v} \ge v^*$, and continued the optimizing process within the respective limits of the constraints. The shape with the highest EI was selected as the final design. This process enabled us to find a shape of the discharge chamber optimized for the given input power $P^*(= J^* V^*$, with the required discharge current J^* and discharge voltage V^*).

VI.   Example of Optimization Calculation

In this study, the optimization was performed to seek maximum thrust efficiencies at discharge voltages of 25-47 V in 1 V increments. Figure 3 shows the calculated thrust efficiencies of 178 chamber shapes in this series.
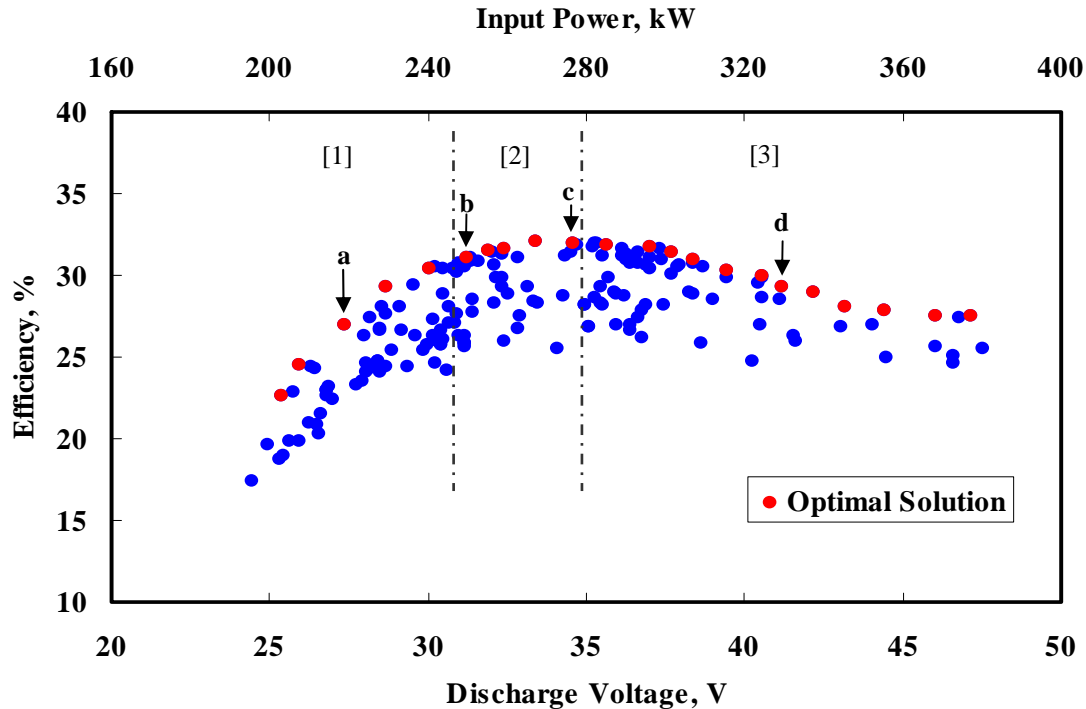

Figure 3. Variation in thrust efficiency with discharge voltage (Ar, 0.8 g/s, 8 kA)

The red points in Fig. 3 show the maximum thrust efficiencies attained at 22 voltage levels. These represent the optimal chamber shapes for each voltage.

Let us consider the variations in thrust efficiencies indicated by the red points. The thrust efficiency shows a large increase in region [1] (about 25-31 V). The variation in thrust efficiency is lower, nearly zero, in region [2] (about 31-35 V). Thrust efficiency then decreases in region [3] (about 35-47 V).

Figure 4 shows an example of the shape of the discharge chamber in region [1], corresponding to point **a**. Similarly, Figs. 5, 6 and 7 show the discharge chamber shapes corresponding to point **b** on the borderline between regions [1] and [2], point **c** on the borderline between [2] and [3], and **d**, respectively.
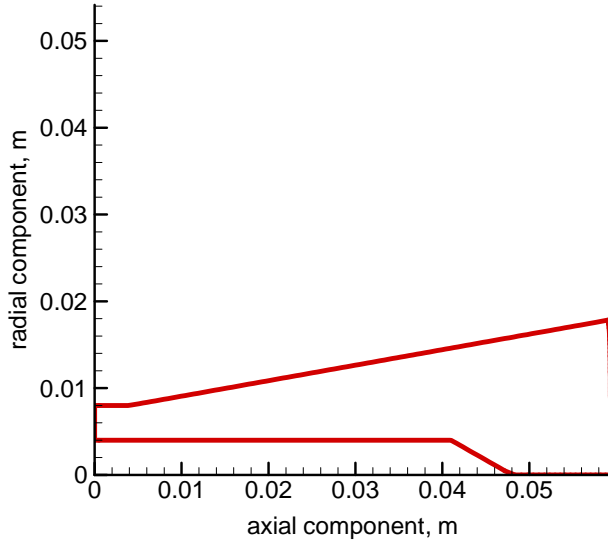
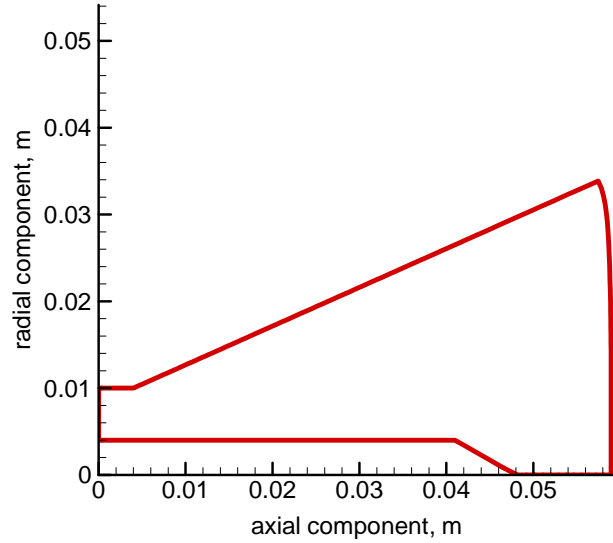**Figure 4. Optimal chamber shape at point a**
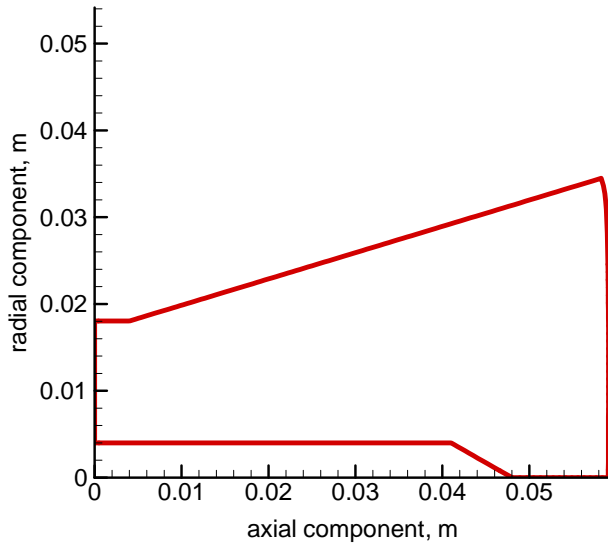

Figure 5. Optimal chamber shape at point b

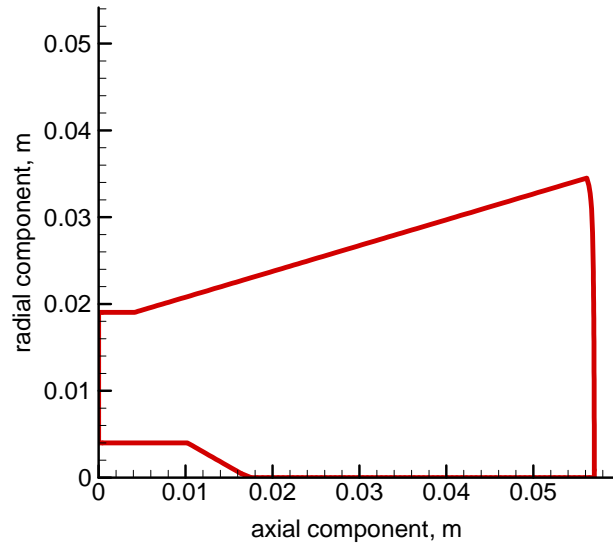

Figure 6. Optimal chamber shape at point c

Figure 7. Optimal chamber shape at point d

A. Variations in optimal discharge chamber shape with discharge voltage

The trend shared by the chamber shapes in all three regions is that the maximum overall chamber length is close to 6 cm. The lengthening of the anode, which also serves as a nozzle, helps to efficiently transform the enthalpy of the plasma flow into kinetic energy. They also shared a tendency for the length of the straight portion to be near the minimum permitted value of 0.4 cm.

Let us now discuss these findings, beginning with region [1], where **a** is defined. The cathode length in this region is nearly constant, near its maximum of 4.8 cm, and the inlet anode radius varies only slightly, generally within the range 0.7-1 cm. What varies most in this region is the outlet anode radius; it rises with increasing discharge voltage to a maximum of 3.5 cm at point **b**.

In region [2], it is mainly the radius of the inlet anode that increases. It reaches 1.8 cm close to its maximum permitted value of 2.0 cm at point **c**. The cathode length remains generally constant in this region.

In region [3], the cathode length gradually diminishes with increasing discharge voltage. The other parameters do not change, with the outlet and inlet anode radii remaining close to their maximum limits.

To summarize the above variations in discharge chamber shape, up to point **c** (i.e., in regions [1] and [2]), the distance between the electrodes increases, with the cathode remaining long while the anode dimensions are vary. Thereafter, in region [3], the inter-electrode distance remains constant while the cathode length is reduced.

B. Variations in thrust efficiency of optimal discharge chamber shape with respect to discharge voltage

Let us consider the causes of the variations in thrust efficiency with discharge voltage seen in Fig. 3. The thrust obtained using Eq. (11) can be divided into two components, magnetic and aerodynamic. Figure 8 presents these two components as they vary in the 23 optimal discharge chamber shapes.
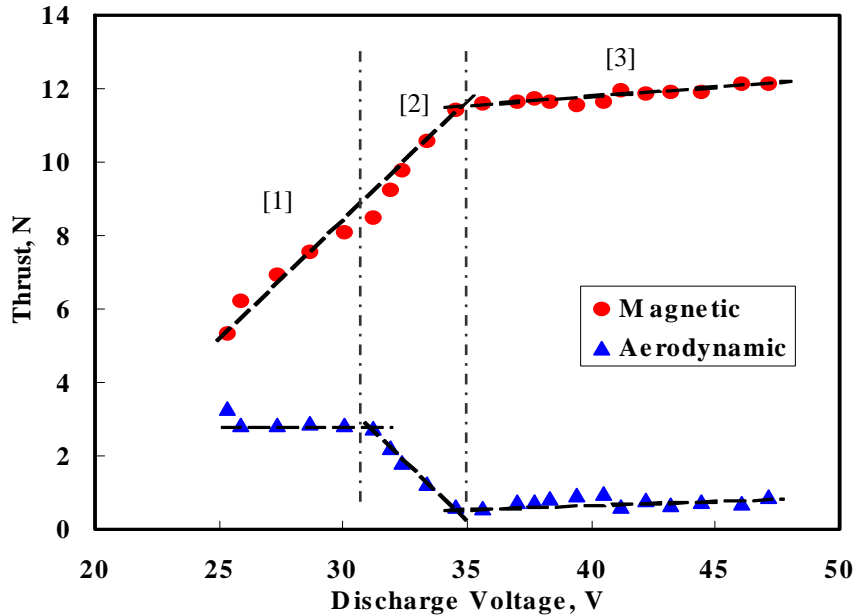

Figure 8. Breakdown of thrust components

As seen in the figure, the magnetic thrust is generally much higher than the aerodynamic thrust. Thus, the magnetic thrust is the dominant component for every chamber shape. At the same time, there are unambiguous differences between the two components in how they vary with discharge voltage.

The magnetic thrust rises relatively quickly in regions [1] and [2]. It then becomes roughly constant in region [3]. This is because the change in the optimal shape of the discharge chamber in these regions is due to increasing inter-electrode distance. Then, the distance is approximately constant at its maximum allowed value in region [3], causing the magnetic thrust to be approximately constant.

In regions [1] and [3], the aerodynamic thrust has nearly constant values of 2.9 and 0.7 N, respectively. Only in region [2] does it change, falling from 2.9 to 0.7 N. The anode radii are fixed in regions [1] and [3] but increase in region [2]. This suggests that the thrust varied in response to the change in inlet anode radius.

In other words, expanding the outlet anode in region [1] increases the inter-electrode distance, also increasing the dominant magnetic component of thrust. The reason to hold the inlet anode radius to a small size in this region is to maintain the aerodynamic thrust at as high a value as possible, obtaining a maximum total thrust. This would explain the increasing thrust efficiency in region [1].

The outlet anode radius size is the maximum possible in region [2]. Therefore, widening the inlet anode increases the inter-electrode distance and, in turn, the magnetic thrust. However, widening the inlet also decreases the aerodynamic thrust, so the growth in overall thrust is not very large. This explains why the thrust efficiency is approximately constant in this region.

Both the outlet anode radius and inlet anode radius are close to their maximum permitted values in region [3], so it is no longer possible to vary the inter-electrode distance, and neither the magnetic thrust nor the aerodynamic thrust change very much.

Also, the discharge voltage rises in region [3] even though the inter-electrode distance does not change. In this region, the discharge voltage is increased by shortening the cathode. The axial and radial components of the Lorentz

The 31st International Electric Propulsion Conference, University of Michigan, USA
September 20 – 24, 2009

force are shown for each discharge chamber shape in Fig. 9, labeled F_z and F_r, respectively, on a cross section on the z-r plane.
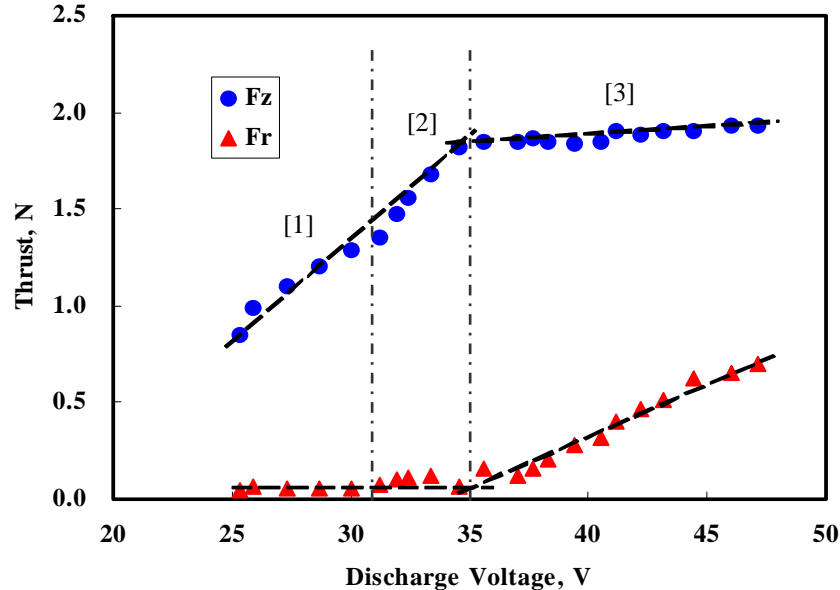

Figure 9. Axial and radial components of Lorentz forces

It can be seen from Fig. 9 that F_r rises with increasing voltage in region [3]. This indicates that shortening the cathode increases the Lorentz force in the radial direction. In other words, raising the radial Lorentz force increases the work for the plasma done by the Lorentz force, which in turn raises the discharge voltage. Thus, in this region, since the inter-electrode distance does not change, the thrust also remains constant. However, shortening the cathode increases the discharge voltage, and this acts to decrease the thrust efficiency.

C. Problems Remaining in our Analysis Code

It was confirmed that the code used in this study to analyze MPD thrusters is reliable for the discharge chamber shape with the flared anode and the short cathode by comparing code results with experimental results. There were some other problems, however, as follows.

I.   Under high input power levels (the region above 40 V in Fig. 3), the calculations for some shapes become unstable, and they diverge under some circumstances. Therefore, the results in this region are somewhat unreliable.

II. The selected discharge current of 8 kA exceeded the critical current for some discharge chamber shapes. It is not appropriate to neglect the Hall effect and other parameters in that region.

III. The discharge voltage was calculated on line integrals from the cathode to the anode. However, there was about a 10% variation in the value found by different integration paths.

Thus, this code leaves some problems yet to be resolved before it is used for complete and total shape optimization.

VII.   Conclusion

This paper proposes the optimization of the discharge chamber cross-sectional shape in the MPD thruster, using a 2-dimensional axially symmetric plasma model, where only flared cross sections of the chamber were allowed. It was shown runs that this optimization process is possible by 178 CFD. The total number of CFD calculations was greatly reduced, indicating that this procedure is feasible for optimizing such chambers in the given problem.

The authors hope to resolve the problems remaining in this analysis code and apply it to discharge chambers of a variety of types besides flared shapes.

Acknowledgments

References

[1]Toki, K., "Optimal Control of Quasi-One-Dimensional Magnetoplasmadynamic Arcjet Flowfields, J. Propul. Power," 13 , 1997, pp. 157-161

[2]Donakd, R. J., Matthias, S. and William, J. W., "Efficient Global Optimization of Expensive Black-Box Functions, Journal of Global Optimization," **13**, pp.455-492, 1998.

[3]Kubota, K., Funaki, I. and Okuno, Y., "Numerical Investigation of Ionization and Acceleration Processed in a Self-Field MPD Thruster," IEPC paper 2005-089, 2005

[4]Chiba, K., Imamura, T., Amemiya, K. and Yamamoto, K., "Design Optimization of Shielding Effect for Aircraft Engine Noise , Journal of Environment and Engineering," **2**, pp.567-577, 2007.

[5]Jeong, S., Murayama, M. and Yamamoto, K., "Efficient Optimization Design Method Using Kriging Model, Journal of Aircraft," **42**, pp 413-420, 2005.

[6]Timothy W. S., Timothy M. M., John J. K. and Farrokh M., "Kriging Models for Global Approximation in Simulation-Based Multidisciplinary Design Optimization," AIAA J., **39**-12, pp. 2233-2241, 2001

[7]Art, B. O., "Orthogonal Arrays for Computer Experiments, Integration and Visualization, Statistica Sinica," **2**, pp.439-452, 1992.

[8]Rainer, S. and Kenneth, P., "Differential evolution – a simple and efficient heuristic for global optimization over continuous spaces", Journal of Global Optimization, **11**, pp. 341–359 (1997).

[9]Nakata, D., Toki, K., Funaki, I., Shimizu, Y., Kuninaka, H. and Arakawa, Y., "Experimental Verification of the Nozzle Shape Optimization for Self-Field MPD Thruster," IEPC paper 2005-163, 2005